Fault imprint in clay units: Magnetic fabric, p-wave velocity, structural and mineralogical signatures

Eva Moreno, Catherine Homberg, Johann Schnyder, Alain Person, Christian David, Arthur Du Peloux, Emeline Moubeche, Audrey Bonnelye, Pierre Dick

Fault imprint in clay units: magnetic fabric, p-wave velocity, structural and mineralogical signatures

Moreno Eva[1,], Catherine Homberg [2], Johann Schnyder[2], Alain Person[2], Christian David[3] Arthur du Peloux[2,4], Emeline Moubeche[2], Audrey Bonnelye[3]and Pierre Dick[4]

1- Sorbonne Université, Faculté des Sciences, MNHN, CNRS, IRD, IPSL, LOCEAN, F-75252 7 Paris, France.eva.moreno@mnhn.fr (corresponding author)

2- Sorbonne Université, Faculté des Sciences, CNRS, ISTeP, F-75252 Paris, France.

3-Université de Cergy-Pontoise, Laboratoire Géosciences &Environnement Cergy (GEC), F-10 95000 Neuville sur Oise, France.

4- Institut de radioprotection et de sûreté nucléaire IRSN/PRP-DGE/SRTG, Laboratoire d' Etude et de recherche sur les Transferts et les Interactions dans les Sols, BP 17, F-92262 Fontenay13 aux-Roses Cedex, France.

1. Introduction

Because of their low permeability properties coupled to a large thickness (several hundreds of meters) and a high sorption capacity, argillaceous formations have been considered as potential host rocks for nuclear waste long-term storage in several countries (Cabrera, 2002; Matray et al. 2007; Sellin and Leupin, 2013). However, faults and fractures in these materials are likely to impair their natural containment capabilities. For this reason, understanding the hydro-mechanical properties and the behaviour of faults in clay-rich sedimentary rocks is a topical subject for better appreciating fluid migration in deep sedimentary basins and the potential loss of integrity as geological barriers (De Barros et al. 2016; Lefevre et al. 2017).

Anisotropy is an important characteristic that influences the clays behaviour. The properties of the argillites normally depend on the process of rock formation (deposition, compaction and diagenesis) but bedding, schistosity, and cleavage also affect the anisotropic character of

the clays. Anisotropy properties of argillaceous formations can be evaluated by conducting the magnetic susceptibility p-wave velocity measurements. In clay-rich sedimentary rocks formations, the anisotropy of magnetic susceptibility (AMS) technique can be used to detect very subtle to strong tectonic deformation, even when they look undeformed at outcrop scale (Parès, 2015). On the other hand, the anisotropy of p-wave velocity (APV) is mainly controlled by the bulk elastic parameters, including the effect of pores, cracks and mineralogical content (Louis et al.2008) and is strongly influenced by deformed structures such as scaly clays, shear bands and microfolds because they are small-scale discontinuities (Jaeggi et al. 2017). Therefore, the AMS and APV are two complementary approaches for understanding the effect of failures, fractures and ductile deformation in the organization of clays. Despite the interest that these two properties have in the integral understanding of the behaviour of the rock in fracturing, there are not many studies in which these two techniques are combined. Louis et al. (2008) characterized the AMS and APV in siltstones and sandstones samples in the Chelungpu fault system (Taiwan). These two techniques were also used to investigate the anisotropic behaviour of the Callovo-Oxfordian argillites (David et al. 2007) but far from a fault core zone.

In addition, the presence of faults and fractures can play an important role in controlling the migration of crustal fluids and therefore mineralogical changes are extremely sensitive to fault architecture. The intensification of the fracture network in the damage zone leads to an increased permeability with respect to the undamaged zone conducting to an authigenic growth of clays and other minerals. Conversely, the fault gouges tend to indicate a general low bulk hydraulic conductivity behaviour (Faulkner et al. 2010; Dick et al. 2016; Lefevre et al. 2016).

Thus, it seems that a close-knit coupling exists between structure, mechanics and fluid flow properties in fault zones (Faulkner et al. 2010). The mechanical properties of the protolith will influence the architecture of the fault zone, which will control the fluid circulation that will itself affect the mechanical properties of the fault zone.

To better understand the interrelationship between fault architecture, petrophysical properties and fluid flow circulation within a fault zone in argillaceous formation, a multidisciplinary study was made in two cores horizontally cores drilled in the Tournemire underground research laboratory (URL) in southern Aveyron (France). We used an integrated approach involving: structural analysis of plane and faults, petrophysical properties (APV and AMS) and mineralogical content.

To our knowledge this is one of the first studies to combine petrophysical and mineralogical properties of samples retrieved across a fault core zone and thus this work provides a unique opportunity to better understand the evolution of structure, petrophysical and fluid flow properties across a fault zone within clay formations. Several important questions will be addressed: Do AMS and APV properties change in phase or is their evolution different with respect to the fault? To what extent are the AMS and APV properties related to tectonic deformation? How much are these properties sensitive to localized deformation? Is it possible to observe a mineralogical change involving the presence of fluid circulation? Is there a relationship between the mineralogical changes and the petrophysical properties of the sediment?

2. Geological and tectonic features

The Tournemire Underground Research Laboratory (URL) is located in the South of France (Aveyron) in the western part of the so-called “Causse du Larzac” (Figure 1). The URL is

operated by the French Institute for Radiological Protection and Nuclear Safety (IRSN), to study the confining properties of an argillaceous formation (Cabrera et al., 1999).

The sedimentary series in this site are composed of a 250 m thick layer of clays and marls (Toarcian and Domerian) bordered by two limestone and dolomite formations (Aalenian/ Bajocian in the upper part, and Carixian/ Sinemurian in the lower part) where two aquifers are present (Cabrera et al., 1999).

Fracturing evolution, associated with the regional tectonic history in the Tournemire area, was described and discussed in detail by Constantin et al. (2002, 2004). To summarize, the tectonic faults and fractures observed in the region are the results of two main tectonic phases: a first extensional tectonic phase, which comprises three episodes during the Mesozoic and a second major tectonic phase occurred during the Eocene associated to the Pyrenean compression.

The argillaceous formation of Tournemire is affected (Figure 1) by the Cernon fault (80 km long) which present a vertical and horizontal offset of several hundreds of meters and the Tournemire fault (11 km long), a local fault associated with compression tectonics (Cabrera, 2002).

In addition, the URL is crossed by two main parallel fault zones (F1 and F2) separated by relatively undeformed rock (Bretaudeau et al., 2014) (Figure 2A). These faults of several hundred-meter length present a small vertical but a larger horizontal displacement (strike-slip faults). The main underground tunnel and several galleries intercept these faults and several boreholes have been drilled by the IRSN. Therefore, the Tournemire URL presents a unique opportunity to study in situ the evolution of the properties of clays with respect to this type of faults.

Previous studies indicate that the F1 and F2 faults show mainly a reverse left-lateral strike slip movement (Peyaud et al. 2006). The fault's strike between N170° to N010° and 60°W to 80°W (Lefèvre et al., 2016).

The sedimentary series have a sub-horizontal bedding which dips gently by 5-10° towards north but it can reach higher bedding dip values at the fault core (Dick et al., 2016). A dolomitic horizon marker crossed by several boreholes on either side of the fault indicated a perpendicular slip perpendicular of around 4–6 m while slip along strike is estimated to be between 15 and 30 m (Dick et al. 2016).

3. Materials and strategy of sampling

We studied two boreholes (called cores in this paper): core TF1 (dip 1°, azimuth 80°N) and core ASM1 (dip 0°, azimuth 70°N). They were respectively drilled in the main tunnel in 1998 and in the "east gallery_03" in 2012 (Figure 1). ASM1 measures 101 mm in diameter and 690 cm in length and was entirely studied. TF1 measures 96 mm in diameter and 2000 cm in length but only the interval between 480 and 1432 cm and between 1578 and 1600 cm was studied. Most of the measurements were done on 2014 and 2015 and until that time, the section cores were kept vacuum sealed in foil to prevent sample alterations.

The architecture of the fault zone F2 has been already characterized in previous papers (Dick et al. 2016, Lefevre et al. 2016). It is characterized by a central fault core and a fractured damage zone. The fault core consists in thin dark bands of centimetre thick gouge, cataclastic and brecciated rocks, as well as sub-vertical schistosity planes, folds and also lenses of less deformed rocks (Dick et al., 2016). The surrounding fractured damage zone is characterized by a dense network of small faults, fractures, and calcite veins. Figure 2B shows an example

of the type of structures that were observed at the damage zone and the fault core zone of the TF1 fault.

The length of each zone in cores TF1 and ASM1 was determined on the basis of the description and the log carried out during the drilling operation (IRSN internal reports) (Figure 3). In both cores, the number of fractures was significantly higher in western side than in the eastern side. In addition, while the boundary between the damage and the fault core zone is sharp, the boundary between the damage and the undamaged zones was vague.

In core TF1, the western and the eastern sides of the core measure respectively 3 m and 1 m and the fault core measures 0.8m. In core ASM1, both sides have a very similar extent of around 2.5m and the fault core measures 1m (Figure 3).

After the macro fracture pattern analysis, the core sections were cut in $2x2x2cm^3$ oriented cubes for the measurement of anisotropy of magnetic susceptibility (AMS, 250 samples) and the anisotropy of P-wave velocity (132 samples). Unfortunately, the section 1380-1406 was too fractured and the preparation of cubes failed.

Samples intended for bulk mineralogical content, clay mineral content and magnetic mineral analysis were obtained differently in the undamaged and the damaged zone. In the undamaged zone, a whole piece of the bulk sediment was cut and crushed in a mortar. In the damage zone and at the fault core fault, the samples were taken along the fracture planes. About 1 mm thick layer, was scratched and crushed in a mortar into fine (bulk mineralogy, magnetic minerals) or coarse (clay minerals content) powders.

4. Results

4.1 Structural analysis

TF1 core is cut by numerous thin fracture planes, most of them showing a well preserved striae (Figure 4A). Most of the brittle deformation within the F2 fault zone thus corresponds to fault planes. Faulting is more intense in the damage zone (67 fractures measured in the western damage zone) than in the fault core (14 fractures measured). Due the absence of weathering, the fault surfaces are exceptionally well preserved enabling to determine the sense of slip. Seventy-six fault slip data, including fault plane and slip vector (striae), were thus collected in TF1 core, as well as five fractures with no or poorly preserved striae as shown in the rose diagram, 85% of the measured fault planes trend between N150°E and N020°E, thereby confirming the N-S orientation of the F2 fault zone and further indicating a moderate variability of the brittle fracture strike within the fault zone.

The fault population collected in TF1 core does not fit with a unique sense of shear, revealing a complex history of F2 fault. Dextral and sinistral movements, as well as normal and reverse movements exist (Figure 4A). The two last types represent 15% and 9% of the fault planes. Strike-slip faults thus represented the majority of the measured planes (76%). Among them, dextral and sinistral faults where found in a similar proportion. The distribution direction has prominent peaks trending at N000°E -N010°E for the sinistral faults, N010°E -N020°E for the dextral and reverse faults, and N020°E -N030°E for the normal faults. This similarity in direction suggest that some faults corresponded to the reactivation of others which is further confirmed by the observation of superposed horizontal and highly dipping striae on several fault planes. The superposition seems non-systematic and a relative age-relation by striae overprinting could not be determined. Despite the age uncertainty, these data indicate that F2 fault zone suffered several periods of activity under different driving stresses. Two strike-slip

regimes, with approximate NE-SW and NW-SE compression, and a normal regime with a WNW-ESE direction of extension are inferred from the orientation of the fault-slips.

The brittle fractures observed in ASM1 core are different than in TF1 core. 64% of the 36 measured fracture planes in ASM1 trend between N100°E and N140°E (Figure 4B). Among the 22 fractures showing a well preserved striae, all but three correspond to reverse faults with a more or less important strike-slip component. The remaining fractures are E-W sinistral faults with or without a normal component (3 data) and WNW-ESE joints (14 data). Observations carried on the gallery walls indicate that an E-W reverse fault exists close to the ASM1 drilling. We therefore suggest that most fractures measured in ASM1 core are related to this second fault. Rare NS planes exist, probably in relation with F2 fault, but this overprinting makes difficult to capture how the architecture of F2 fault evolves from ASM1 to TF1 drilling.

As far as the fault dips are concerned, most of the N-S fault planes collected in TF1 core, whatever their movement, show value between 5° to 45° (Figure 4A). This moderate dips are rather surprising for a strike fault zone and constitute a major structural element of F2 fault. Several mechanisms may explain these unexpected fault dips. Post- faulting local or regional tilting may have later modified the fault attitude but can be excluded here because the bedding dip does not exceed 10° and because faults have no preferred inclination polarity, dipping either to the west or to the east. An alternative scenario is that F2 fault formed as a normal fault, with eventual flattening of the brittle planes due to compaction, and was later reactivated as a strike-slip fault. Following the paleostress reconstitution of Constantin et al. (2004) , the direction of extension during the Mesozoic rifting trended E-W and the direction of the Eocene compression switched from NE-SW to NW-SW direction. Such a stress succession would cause first normal slip, then dextral slip, and finally sinistral slip on F2

fault. Observations of these three types of fault movement in TF1 core suggests that F2 fault zone have suffered several periods of activities, in relation with the tectonic phases that affected the region during Meso-Cenozoic times. Alternative scenario, implying contemporaneous slips, is further developed in the discussion.

4.2 Anisotropy of magnetic susceptibility

The anisotropy of magnetic susceptibility (AMS) can be represented as a second order symmetric tensor that can be represented geometrically as an ellipsoid with three principle susceptibility axes: maximum (K1), intermediate (K2) and minimum (K3) susceptibility with mean magnetic susceptibility Km=(K1+K2+K3)/3. The AMS was estimated using a Geofyzika KLY-3 KappaBridge at the Paleomagnetism laboratory in the *Institut de Physique du Globe de Paris* (IPGP) (France).

The range of susceptibility values found in the Tournemire sediments are comprised between 135 and 200×10^{-6} SI which suggests an important contribution of paramagnetic minerals (mainly clays). Thus, the AMS ellipsoids reflect mainly the preferred orientation of clay minerals, and can be used to investigate tectonic-related fabrics (Cifelli et al., 2009; Mattei et al., 1997; Parés et al., 1999). When normalized by the density (mass magnetic susceptibility), these values ranged between 60 and 80×10^{-9} m^3/kg (Figure 5). We observed that, while in TF1 the susceptibility presented a normal distribution, a bimodal distribution was observed in ASM1. Mean values on the east (E) block of the fault were lower than in the west (W) block (Figure 5). The difference in magnetic susceptibility values between the east and west blocks could be related to the presence of calcite, a diamagnetic mineral. According to the mineralogical analyses carried out, the calcite content is higher in the eastern side.

Jelinek (1981) introduced different parameters to interpret the degree and shape of the anisotropy of magnetic susceptibility: lineation (L=K1/K2); foliation (F=K2/K3). The shape parameter (T) combines the lineation and foliation parameters ($T = ((\ln L - \ln F)/(\ln L + \ln F))$. Positive T-values imply an oblate ellipsoid, negative values imply prolate ellipsoid, and T-values close to zero imply neutral ellipsoids. Finally, Pj is the corrected degree of anisotropy ($Pj= \exp(\sqrt{2[(\ln(K1/km)^2+\ln(K2/km)^2+\ln(K3/km)^2]})$. Higher Pj values imply increasing strength of the ellipsoid shape.

The evolution of magnetic fabric along the cores was inferred by the Jelinek diagram (T versus Pj) (Figure 5) and by the equal-area, lower-hemisphere projection of the K1 and K3 axes using the Anisoft software (Figure 6). A bedding plane dip of 10° towards the north is reported that corresponds to the measurements estimated by Dick et al. (2016) in the undamaged and damage zone at the west side of the fault.

With the increasing tectonic deformation, the evolution of the magnetic fabric can follow different stages (Borradaile and Henry, 1997; Parés et al. 1999; Parés 2004, 2015): The type I corresponds to the sedimentary fabric and is characterized by the K3 axes perpendicular and the K1 axes are distributed on the bedding plane without a predominant magnetic lineation. The *Pj–T*diagrams show magnetic fabrics characterized by strongly oblate shaped susceptibility ellipsoids. If the sediments are deposited under a weak current flow, the K1 axes can be aligned parallel to the paleocurrent flow azimuth.

Type II corresponds to a weak-moderate deformation with the K3 axes perpendicular to the bedding plane and the K3 axes parallel to the extensional direction. Type III, corresponding to a high deformation stage. The K3 axes show a girdle that is parallel to the maximum shortening direction and the K1 axes perpendicular to it. Furthermore, the *Pj–T* diagrams

show a neutral ellipsoid that could be developed due to tectonic compression. The last stage of deformation (type IV) is reached when K3 is within the bedding plane and the ellipsoid is prolate.

In the undamaged zone of core TF1, the AMS ellipsoid had a predominantly oblate shape with a magnetic foliation parallel to the bedding plane (Figure 6). The shape of AMS ellipsoid at this zone had a generally oblate shape with a low degree of anisotropy (Figure 5) and the maximum axes are relatively well clustered with a general NE–SW orientation. An oblate fabric was also observed in the damage zone. In this case the K1 axes are rotated in anti-clockwise direction. and the minimum K3 axis had a lower inclination values (75-80°) that can be explained by the observed increase in bedding plane dip towards the fault core (Dick et al. 2016). Within the fault core, the AMS ellipsoids had very different signatures in sections 1353-1380 cm (west side) and 1406-1432 cm sections (east side). In section 1353-1406 cm, we can observe a type III fabric, the minimum K3 axes are distributed around a girdle from the vertical to the horizontal plane and the maximum K1 axes follows a NW-SE orientation. In addition, the Jelinek diagram (Figure 5) shows a strong decrease of the anisotropy degree (P) and a change of the magnetic shape factor (T) from high oblate (T~1) to neutral (T~0).

The samples from section 1406-1432 section revealed also a girdle distribution of the K3 axes but the K1 axes follow a NE-SW direction. The Jelinek diagram indicates an oblate fabric.

Conversely, in ASM1, the magnetic fabric was very similar in the damage and the fault core. It was characterized by an inclination of the K3 axes of 75-80° and an orientation of the K1 axes towards a NW-SE direction (Figure 6). We didn’t observe the developpement of a type

III fabric but the Jelinek diagram (Figure 5) shows a slight decrease in T from 1 to moderate values (T~0.5) indicating a weak deformation stage. In addition, we also observed higher degree of anisotropy (Pj) at the E-block. This part of the fault is also characterized by lower magnetic susceptibility (Figure 5 and Figure 7).

4.3 Anisotropy of P-wave velocity

The P-wave velocity (V_P) was measured on the cubes from both cores TF1 and ASM1 along the three axes x, y and z using ultrasonic transducers with dominant frequency 1 MHz, a Panametrics 5058 PR pulser and a digital oscilloscope. The velocity is conventionally inferred from the travel time for a wave propagating from the transmitter to the receiver. Previous works showed that compressional wave velocity is inversely correlated to total porosity and clay mineral contents (Han et al., 1986). In addition, in normal consolidated sediments, the Pwave velocity is faster in the bedding plane than perpendicular to it.
The anisotropy of P-wave velocity (APV) is defined as the difference between maximum and minimum velocities normalized to the average velocity:

APV(%)=100*(Vp max-Vp min)/Vp mean, where Vpmin is the P-wave velocity in the Z direction (VPz), perpendicular to bedding, and Vpmean the average velocity in the bedding plane (Vpx+Vpy)/2. The Vp mean, Vpz and the APV (%) are shown in Figure 7. The P-wave velocities in the bedding plane were much higher than the vertical one and lead to large APV values of around 50% in the undeformed zone to around 40% in the damage zone. In core TF1, we observed a drastic change within the fault core with a strong dispersion of APV values down to negative values, reflecting elastic anisotropy reversal. This is mainly due to the increase in P-wave velocity along the vertical axis and a decrease in the horizontal axes. Such a change is not observed in the fault core of ASM1. We can observe that in general the

276 changes in the P-wave velocity and the APV are in phase with changes the AMS properties
277 (Figure 7).

278 4.4 Clay minerals assemblages and bulk mineralogy

279 Bulk mineralogy and clay mineral assemblages were identified using X-ray diffraction
280 (XRD). It should be remembered that the samples for the XRD and MEB measurements
281 come from a block of total sediment in the undamaged zone and from the first millimetres
282 along the slip planes from fractures in the damage zone and in the fault core.
283 XRD samples were prepared according to the powder diffraction method (Brindley and
284 Brown, 1980). For clay mineral preparation, we followed the analytical procedure of
285 Holtzapffel (1985). X-ray diffractograms were obtained using a D2 Brucker diffractometer
286 equipped with a Lynx Eye detector, with CuKα radiation and NI filter. Measurement
287 parameters were as follows: 2.5 to 35° (2θ), in steps of 0.02° each 0.2 s. The identification of
288 clay minerals was made according to the position of the (001) reflections of the X-ray
289 diffractograms (Brindley and Brown, 1980; Moore and Reynolds, 1989) using a MacDiff
290 software.
291 XRD analysis was complemented by the analysis of some bulk samples from the undamaged
292 host rock and fractures planes within the damage zone in a scanning electron microscopy
293 coupled to an energy-dispersive X-ray spectrometry system (SEM-EDS). We used a ZEISS
294 supra V5 instrument provided with a BRUKER detector in energy dispersive spectroscopy
295 (EDS) at the Petrology, Geochemistry, Magmatic Mineralogy Laboratory (PG2M) ISTEP of
296 the University Pierre and Marie Curie (Paris).
297 The major mineral assemblages identified by XRD analysis were clays (18-48%, mean
298 37%), quartz (21-48%, mean 37%) and calcite (9-61%; mean 27%). Pyrite and siderite were
299 found as secondary minerals with concentrations below 5% and they were not quantified. We

observed small quantities of ankerite and ferroan dolomite both in the undeformed host rock sediment and in the damage zone by SEM-EDS (Figure 9). This finding is in agreement with previous studies (Lerouge et al., 2012; Peyaud et al., 2006). We must note that core TF1 was drilled in 1999 and that some mineralogical alteration could have occurred. However, its composition is similar to the one in core ASM1, collected 14 years later indicating that post-drilling alteration didn't change the original mineralogical composition.

The calcite content in the western undamaged zone is very low (~15%) (Figure 8) and corresponds to the average calcite content estimated in the Tournemire site (Boisson et al. 1996). As we approach the centre of the fault, the calcite content from slip planes showed very scattered values (10-60% in core TF1 and 9-51% in core ASM1) indicating that some fractures are filled with calcite cement and some other are not. This calcification took place during two episodes of compressive deformation during the Pyrenean orogeny (Lefèvre et al., 2016).

Additionally, we also observed higher $CaCO_3$ content in the eastern compartment (30-35%) (end of damage zone and undeformed zone), reaching 30-35% (Figure 8). We interpret that this increase is not caused by precipitations from tectonically induced fluids (macroscopically, we found no veins in this core section/ these samples) but that it rather indicates a different background signature for calcite content eastwards of the fault zone.

Average proportions of the various clay species in TF1 and ASM1 cores are very similar (Figure 8). The clay mineral assemblage in core TF1consisted of illite (35 to 45%, near 40% on average), kaolinite (25 to 40%, 33% on average), illite-smectite mixed layers (I/S, 15 to 25%, 19% in average) and chlorite (5 to 10%, 9% in average).

322 The clay mineral assemblage in core ASM1 consisted of illite (5 to 40%, 36% on average),
323 kaolinite (30 to around 40%, 34% on average), I-S (15 to 35%, 21% on average) and chlorite
324 (5 to 10%, 9% on average).
325 Clay mineral proportions in TF1 and ASM1 cores were also very similar to the ones
326 previously determined at Tournemire site (Savoye et al.,2008; Dick et al. 2016). However,
327 while Savoye et al. (2008) didn't show any significant change in the clay assemblage as
328 function of the distance to the fault plane, our results revealed a weak but noticeable increase
329 in kaolinite (Figure 8). The maximal difference in kaolinite content between the undamaged
330 and the fault core zones is 14% in core ASM1 and 9%, in core TF1, slightly higher than the
331 analytical error (±5%). We interpret this mineralogical evolution as significant as the same
332 mineralogical trend is observed in both ASM1 and TF1 cores toward the deformed zones. A
333 previous work indicates that the proportion ok kaolinite, can be even higher (63-72%) when
334 we look at the fault gouge (Dick et al. 2016). Such a kaolinite increase toward the fault core
335 has been considered to reflect a high degree of fluid–rock interaction (Rossetti et al. 2010).
336 An additional mineralogical change recorded in our data set ASM1 (Figure 8) is
337 characterized by a large increase in I/S proportions correlated with a decrease in illite from
338 the fault core boundary (I/S 16% and illite 42%) to the eastern undamaged zone (I/S 35% and
339 illite 23%). This sharp mineralogical change may suggest a vertical offset that can be more
340 important in ASM1. After the difference in the dolomitic horizon marker observed on either
341 side of the fault, suggest that the amount of the perpendicular slip is of around 4–6 m (Dick et
342 al. 2016).

343 4.5 Magnetic mineralogy based on low temperature SIRM

344 Low-temperature isothermal remanence magnetizations (LT-SIRM) were made in core TF1
345 using a Quantum Design Magnetic Property Measurement System (MPMS2) SQUID

magnetometer at the IPGP Paleomagnetic laboratory in Paris (France). The powders used for these analysis were collected on the fault planes and fractures at different points of core TF1 with the exception of the sample in the undeformed zone which comes from the bulk sediment.

Two different LT-SIRM experiments were performed. First, samples were cooled in zero field to 10 K, and a magnetic field of 2.5T was given at 10 K. The SIRM was measured in approximately zero field at 5-K intervals up to 300 K (zero-field cool curves, ZFC). In the second experiment, the samples were cooled in a high magnetic field of 2.5 T and then the SIRM was measured again every 5K up to 300 K (field-cool curves, FC).

We observed two transitions in the ZFC and FC curves: A small drop at 120 K, in the majority of the samples (sometimes only observed in the first derivate curves) which corresponds to temperature of the magnetite Verwey transition, Tv (Verwey, 1939) (Figure 10). The elevation of FC SIRM over ZFC SIRM and the small loss in remanence across the Tv warming indicates a very fine grain-size, lower than 0.1µm which correspond to single-domain (SD) magnetite (Özdemir et al., 2002; Smirnov, 2009). In addition, a linear decrease trend observed in the FC and ZFC SIRM curves above the Verwey transition (T > 120 K) indicates the presence of superparamagnetic (SP) grains. The frontier between the SP and SD grains depends on the shape of magnetite but for detrital magnetite with isotropic grains, the limit is at around 0.017 µm (Muxworthy and Williams, 2009).

In addition, magnetite is characterized to have a high remanence at room temperature and we used the SIRM at 300K ($SIRM_{300K}$) to evaluate the evolution of magnetite content along the TF1.

A second large drop in remanence was observed around 35K and it was related to the Neel transition of siderite. Siderite is also characterized by a FC remanence below 40K much larger than the ZFC remanence (Housen et al. 1996).

Two other minerals have magnetic transitions around 35K: rhodochrosite ($MnCO_3$) whose Neel temperature is 32K (Housen et al., 1996) and pyrrhotite ($Fe_{1-x}S$) which has a magnetic transition at 35 K (Dekkers et al., 1989; Rochette et al., 1990) now known as Benus transition (Rochette et al., 2011). Aubourg and Pozzi (2010) as well as Aubourg et al. (2008) attributed the drop in the ZFC/FC curves in samples from Mont Terri Lower Dogger claystones to a combination of paramagnetic input (clay minerals), pyrrhotite transition and the effect of superparamagnetic grains (SP). However, in Tournemire site, pyrrhotite wasn't found neither by XRD analysis nor SEM/EDS observations while siderite can be detected by XRD and have concentrations lower than 5%.

The magnetic mineralogy evolution from the undeformed host rock to the fault core was studied using the $SIRM_{300K}$ used as an estimate of fine-grained magnetite and FC/ZFC ratio at 10 K, used to indicate the occurrence of siderite. For pure siderite, the difference is higher than 10 (Frederichs et al., 2003; Housen et al., 1996).

We observed a sharp increase in the $SIRM_{300K}$ values in the damage zone (Figure 10) in phase with a decrease in the FC/ZFC_{10K} ratio. These changes were interpreted as a partial oxidation of siderite to magnetite due to the presence of fluid circulations (Ellwood et al., 1986).

5. Discussion

The multi-proxies approach used in this study confirmed the commonly accepted zooning along a fault zone: an undamaged area characterized by samples with little or no fracturing, a

391 damage zone with a large number of calcified fractures and a fault core characterized by high
392 deformation and no apparent bedding. Based on this finding, it is tempting to assume a fault
393 zone evolution where a tectonic rework of the host rock lead to the formation of gouge,
394 which we assume to accommodate the largest part of the faults' offset (Dick et al., 2016.
395 Laurich et al. 2018).

396 Our work indicates three main findings:

397 - The tectonic analysis of fractures indicated that the F2 fault underwent a polyphased
398 evolution with reactivations under different tectonic regimes. Two strike-slip regimes,
399 with approximate NE-SW and NW-SE compression, and a normal regime with a WNW-
400 ESE direction of extension are inferred from the orientation of the fault-slips. Most of the
401 N-S fault planes collected in TF1 core, whatever their movement, show dip values
402 between 5° to 45°. This finding constitutes a major structural characteristic of F2 fault.
403 - Second, our study demonstrated that the anisotropy of P-wave velocity (APV) and of
404 susceptibility (AMS) follows the fault zoning in agreement with the results obtained by
405 Bonnelye (2016). We observed the loss of the primary sedimentary fabric in the damage
406 zone and an important decrease in the anisotropy of magnetic susceptibility (AMS) and
407 the P-wave velocity (APV) within the fault core, especially in TF1 core.
408 - Third, we identified evidence of neo-formation of fine-grained magnetite (only measured
409 in core TF1), precipitation of millimetric to infra-millimetric calcite veins and a potential
410 neoformation of kaolinite within the fault planes in the damage and the core fault.

411 ### 5.1 Polyphased fault zone development

412 Fault data collected along the F2 fault evidenced the complex nature of the damage zones of
413 this fault. The damage zones include individual fractures with horizontal and dip slip

movements, sometimes in opposite directions. The NS+- 20 sinistral slip surfaces observed in this study are in agreement with a left lateral movement observed on other segments of F2 fault in the Tournemire URL (Constantin et al., 2002; Lefèvre et al., 2016).

Sinistral and reverse faults in TF1 both indicate a local N130°E σ_H (maximal horizontal stress) and a N040°E σ_h (minimal horizontal stress), in agreement with the N130°E compression inferred from fault-slip data inversion close to the northern continuation of F2 in the western gallery (Constantin et al., 2002). Dextral faults result from a N45°E σ_H and N135°E σ_h. A rather similar WNW-ESE σ_h is inferred from the normal faults and is associated with a normal stress regime.

We propose two different scenarios that may explain this tectonic complexity (Figure 11). We consider (1) a long lived scenario, with fault activity starting in Mesozoic time and regional stresses changing through time (Figure 11A), and (2) a short scenario, in which the fault internal architecture evolved progressively during the displacement accumulation (Figure 11B). Scenarios between these two end member models may further exist. In scenario 1 (Figure 11A), the F2 fault initiated as a normal fault during Mesozoic time under a WNW-ESE extension. As such an extension regime is active during the Toarcian (Constantin et al., 2002), normal faults in Tournemire may predated sedimentary compaction. Subsequent, the F2 fault registered a first dextral slip and a later sinistral one in Eocene time during the Pyrenean orogeny. These two opposite slips result from the counter clockwise stress rotation of the Pyrenean compression, from a N20°E to a N160°E direction (Constantin et al., 2002). In scenario 2 (Figure 11B), the F2 fault observed in the gallery section is a linking fault in an extensive relay between two NNW-SSE dextral faults formed during the Pyrenean orogeny. The normal faults recognized in the TF1 core formed when these two dextral segments were linked (Figure 11B1). Such a development is confirmed in analogue models (Rahe et al.,

438 1998). In the latest stage, the strike-slip fault cut the relay (Figure 11B2) and formed the F2
439 fault. The relay zone was later reactivated as a sinistral strike-slip fault in response to the
440 counter clockwise rotation of the Pyrenean compression (Figure 11B3).
441 Both scenarios are in agreement with the sinistral reactivation of previously dextral faults
442 observed by Lefevre et al. (2016) along another section of F2 fault. Interestingly, the earlier
443 dextral slips are more preserved in the studied portion of the fault zone (50% of the measured
444 fault surfaces in TF1 core). The left lateral reactivation of the fault requires that N160°E
445 compression was deflected close to the fault in order to have a sufficient shear stress.
446 Accordingly, the local stress tensor obtained by Constantin et al. (2002) in the Tournemire
447 gallery indicates that the compression adopted here a N130°E strike.

448 5.2 Fault zoning and longitudinal heterogeneity of anisotropy of p-wave velocity and
449 magnetics susceptibility

450 We found an excellent correlation between the anisotropy of magnetic susceptibility (AMS)
451 and the P-wave velocity (APV) in cores TF1 and ASM1. In the case of argillites, the
452 susceptibility and P-wave velocity are mainly controlled by the preferred orientation of the
453 clay sheets and explains while the magnetic and elastic results converge (David et al., 2007).

454 The results of AMS in ASM1 and TF1 cores indicate that there is a dominance of type II and
455 type III fabrics with oblate to neutral ellipsoids. A magnetic lineation trending NW-SE was
456 observed in the damage zone and in majority of the samples of the fault core zones. Following
457 Mattei et al. (1997) and Parés (2004), this magnetic lineation is usually developed parallel to
458 the extension direction. The observed K1 preferred orientation can result from strike-slip
459 regime with σ_1 trending NE-SW. Such stress state is in agreement with the numerous dextral
460 slip measured in the fault zone. The AMS fabric was thus acquired during the dextral

movement along F2 fault during the Pyrenean orogeny. The normal movement, whatever their age, may also have produced the magnetic fabric, but its contribution is thought to have been less important.

Interestingly, the magnetic fabric in section 1402-1432 in the TF1 core showed a different pattern. In this case, the K3 axes formed a girdle in the NW-SE direction and the K1 axes were preferably oriented in the NE-SW direction. Several mechanisms could explain this change. It could indicate that the eastern side of the fault imprints the deformation due to sinistral reactivation of previously dextral faults. This fabric was also observed in this section. It would be necessary to study other parts of the fault to affirm or decline this hypothesis. On the other hand, AMS tectonic fabric is very sensitive to localized deformation zones such as gouge or deformation bands that are very abundant in this part of the fault. The impact of these deformations on the AMS fabric is an issue that needs to be further explored (Parés, 2015).

Similarly, a complete reversal of elastic anisotropy (APV <0) was also observed within the fault core. Recent experiments on Tournemire shale (Bonnelye et al., 2017) and creep tests (Geng et al., 2017) show an inversion of elastic anisotropy in samples deformed perpendicularly to bed changes due to mineral rotation near fault zones. A tectonic fabric is also detected in a borehole from the Mont Terri rock laboratory thanks to a decrease in the p-wave velocity (Jaeggi et al., 2017).

Thus, the petrophysical results observed within the fault core of TF1 were interpreted as the result of an intense damage process. Here, the bed is only preserved in centimetre -thick zones (Lefevre et al. 2016) which may explain why the % APV and K3 axes showed such

scattered values (Figure 7), these parameters being particularly sensitive to bedding orientation.

Another important result is that the preferred orientation of the K1 axes in the undamaged zone (only available in TF1) was in the NE-SW direction. One possible mechanism is that the alignment of the K1 axes in the undamaged zone is due to a deposition under the influence of a bottom current. In this case, the direction of the K3 axes is perpendicular to the bedding plane and the K1 axes are parallel to the current direction (Beckers et al. 2016; Singsoupho et al. 2015; Parès et al. 2007). Further studies will be necessary to confirm this hypothesis. In ASM1, the AMS and elastic anisotropy didn't show such drastic changes in the fault core. The AMS analysis indicated a type II tectonic fabric (Parés, 2015) and a slight decrease in the p-wave velocity at 300 cm within the fault core. In the fault core, the sediment is characterized by small deformed volumes, shear zones, shear bands and gouge intercalated with apparently undeformed sediment (Laurich et al. 2017; Dick et al. 2016; Lefevre et al. 2016). Despite the care we took in the sampling procedure, the number of sampled cubes were limited by the large number of fractures and it cannot be totally ruled out that the deformation of these relatively small volumes zones were less reflected in ASM1 because they couldn't be sampled. The magnetic fabric in the damage and the fault core in ASM1 show however a similar a preferred orientation of the K1 awes in the NW-SE direction in agreement with the dextral strike-slip regime.

Finally, one of the major characteristic found in core ASM1 was the dissymmetry observed in P-wave velocity, magnetic susceptibility and Pj between the western and eastern parts of the fault. The observed differences seem to be related to a mineralogical change and not to strain and they were not observed in TF1. Mineralogical analysis indicates higher calcite

content in the eastern side and an increase in illite-smectite mixed layers towards the east. As the core was drilled horizontal to the bedding plane, the stratigraphic level (and therefore the mineralogical composition), should be the same on both sides of the fault, unless there is a vertical offset. This vertical offset was observed by Dick et al. (2016). We cannot however quantify it.

5.3 Fluid circulation in the fault zone

The XRD analyses showed evidence of precipitation of millimetric to infra-millimetric calcite veins and a potential neoformation of kaolinite along the fault planes in the damage zone/fault core zones. This was already observed in a previous study of Tournemire shales which indicated that maximum kaolinite content was observed in the fault gouge (Dick et al., 2016). The increase of kaolinite abundance towards the fault core suggests a high degree of fluid–rock interaction (Rossetti et al., 2011).

In addition, the LT-SIRM measurements enabled the identification of small amount of siderite in our samples. Siderite was also identified by XRD but it was not quantified by XRD because its concentration was less than 5%. However, magnetic measurements like SIRM are able to detect ferrimagnetic minerals that are undetected by traditional mineralogical analyses such as XRD, even when the concentrations are as low as 1 ppm (Lagroix, F. and Y. Guyodo, 2017).

Besides, the $SIRM_{300k}$ and FC/ZRC record indicated an increase in fine-grained magnetite and a decrease in siderite towards the damage/fault core boundary (Figure 9).

In Tournemire shales, the fluid circulation mainly occurs between the fault core and the damage zone (Guglielmi et al., 2015; Lefèvre et al., 2016) in which the porosity reaches maximum values (Dick et al., 2016). Therefore, the transformation of siderite into magnetite

seems to be a good index of paleo-fluid circulation and indicates a change in redox conditions related with episodic connections with less reduced fluids from the overlying aquifer (Peyaud et al., 2006). We suggest however the prevalence of reducing conditions, as at higher oxidation rates, the final product of siderite will be hematite instead of magnetite (Ellwood et al., 1986). The presence of minerals like ankerite, calcite, ferroan dolomite and framboidal pyrite observed in the SEM (Figure 8) supports also the prevalence of reducing conditions and were also observed by Peyaud et al. (2006) and Lefèvre et al. (2016).

6. Conclusions

The integrated study of the N-S F2 fault cutting the Toarcian shale formation from the Tournemire Underground Research Laboratory (URL) made it possible to highlight the existing relationships between the fault architecture and its tectonic history with the variations of petrophysical properties (anisotropy of magnetic susceptibility and P-wave velocity) and mineralogy ($CaCO_3$, clays and magnetic mineralogy).

The fault surfaces within the fault zone pointed out that the F2 fault suffered a polyphased tectonic history, with successive reactivations under normal and strike-slip regimes. Notably, slips on fault surface within the damage zone occurred mostly on shallow or very shallow (5° to 45°) dipping N-S fault planes.

Our study demonstrated that the anisotropy of P-wave velocity (APV) and of susceptibility (AMS) are well correlated and they follow the fault zoning. In the damage zone, changes in the ASM and APV properties were mainly related to an increase in the bedding plane dip. Within the fault core zone, a strong anisotropy reversal was observed which indicated a strong sediment deformation and suggest clay platelets rotation near failure. These deformations are however located in very small volumes (deformed bands and gouge).

The observed NW-SE magnetic lineation in both cores ASM1 and TF1 was acquired during the first dextral slip during the Pyrenean orogeny.

The magnetite and potential kaolinite neoformation attest of fluid circulation at the vicinity of the damage/fault core boundary and suggest that the transformation of siderite in magnetite may be a good index of paleo-fluid circulation.

The variability of the response observed in the two studied cores suggests the need to study the characteristics of the fault both across its different architectural zones and along the main fracture plan.

Acknowledgment

This work was funded by a collaboration contract between the IRSN, the CNRS and the MNHN (number DAFCJ/SL/BL-11831). We are grateful to France Lagroix for allowing us the access to the Paleomagnetism laboratory of the IPGP for the susceptibility measurements and for her support given during the low-T SIRM measurements. We are grateful and to Omar Boudouma for his support given during the SEM sessions and for Frederic Delbès in helping for clay mineral analyses. We thank Ben Laurich and the anonymous reviewer for their constructive criticism of the paper.

References

Aubourg, C., Pozzi, J.-P., 2010. Toward a new < 250 °C pyrrhotite–magnetite geothermometer for claystones. Earth and Planetary Science Letters 294, 47-57.

Aubourg, C., Pozzi, J.P., Janots, D., Sahraoui, L., 2008. Imprinting chemical remanent magnetization in claystones at 95 °C. Earth and Planetary Science Letters 272, 172-180.

Beckers, A., C. Beck, A. Hubert-Ferrari, E. Tripsanas, C. Crouzet, D. Sakellariou, G. Papatheodorou and M. De Batist, 2016. Influence of bottom currents on the sedimentary processes at the western tip of the Gulf of Corinth, Greece. Marine Geology 378: 312-332.

Boisson J-Y., Cabrera J. and D. W. L. (1996). Caractérisation des propriétés de transferts au laboratoire des argilites et marnes toarciennes de Tournemire, IRSN report.

Bonnelye, A., 2016. Etude des propriétés physiques et mécaniques des argilites : de la déformation en laboratoire aux failles naturelles. Thèse de doctorat en Sciences de la terre et de l'univers. Université de Cergy-Pontoise.

Bonnelye, A., Schubnel, A., David, C., Henry, P., Guglielmi, Y., Gout, C., Fauchille, A.L. and Dick, P., 2017. Elastic wave velocity evolution of shales deformed under uppermost-crustal conditions, Journal of Geophysical Research., 122, 130-141.

Borradaile, G.J., Henry, B., 1997. Tectonic applications of magnetic susceptibility and its anisotropy. Earth-Science Reviews 42, 49-93.

Bretaudeau, F., Gélis, C., Leparoux, D., Brossier, R., Cabrera, J., Côte, P., 2014. High-resolution quantitative seismic imaging of a strike-slip fault with small vertical offset in clay rocks from underground galleries: Experimental platform of Tournemire, France. Geophysics 79, B1-B18.

Brindley G.W., Brown G., 1980. Crystal structures of clay minerals and their X-ray identification. Mineralogical Society - London.

Cabrera, J., P. Volant, C. Baker, W. Pettitt and R. P. Young, 1999. Structural and geophysical investigations of the EDZ (Excavation Disturbed Zone) in indurated argillaceous media: The tunnel and the galleries of the IPSN Tournemire site, France, American Rock Mechanics Association.

Cabrera, J., 2002. Caractérisation des discontinuités en milieu argileux (station expérimentale de Tournemire). Questions clés relatives à l'évaluation de la sûreté du stockage des déchets radioactifs, Rapport scientifique et technique. Institut De Radioprotection et de Sûreté Nucléaire, pp. 227-232.

Cifelli, F., Mattei, M., Chadima, M., Lenser, S., Hirt, A.M., 2009. The magnetic fabric in "undeformed clays": AMS and neutron texture analyses from the Rif Chain (Morocco). Tectonophysics 466, 79-88.

Constantin, J., Vergély, P., Cabrera, J., 2002. Tectonic evolution and related fracturing in the Causses Basin (Aveyron, France) : the Tournemire area example. Bulletin de la Societe Geologique de France 173, 229-243.

Constantin, J., Peyaud, J.B., Vergély, P., Pagel, M., Cabrera, J., 2004. Evolution of the structural fault permeability in argillaceous rocks in a polyphased tectonic context. Physics and Chemistry of the Earth, Parts A/B/C 29, 25-41.

David, C., Robion, P., Menéndez, B., 2007. Anisotropy of elastic, magnetic and microstructural properties of the Callovo-Oxfordian argillite. Physics and Chemistry of the Earth, Parts A/B/C 32, 145153.

De Barros Louis, Daniel Guillaume, Guglielmi Yves, Rivet Diane, Caron Hervé, Payre Xavier, Bergery Guillaume, Henry Pierre, Castilla Raymi, Dick Pierre, Barbieri Ernesto and G. Maxime, 2016. Fault structure, stress, or pressure control of the seismicity in shale? Insights from a controlled experiment of fluid- induced fault reactivation. Journal of Geophysical Research: Solid Earth 121(6): 4506-4522.

Dekkers, M.J., Mattéi, J.L., Fillion, G., Rochette, P., 1989. Grain-size dependence of the magnetic behavior of pyrrhotite during its low-temperature transition at 34 K. Geophysical Research Letters 16, 855-858.

Dick, P., Wittebroodt, C., Courbet, C., Rvi, J.S., Estève, I., Matray, J.-M., Siitari-Kauppi, M., Voutilainen, M., Dauzères, A., 2016. The internal architecture and permeability structures of faults in shale formations. The Clay Minerals Society Workshop Lectures Series 21, 219-229.

Ellwood, B.B., Balsam, W., Burkart, B., Long, G.J., Buhl, M.L., 1986. Anomalous magnetic properties in rocks containing the mineral siderite: Paleomagnetic implications. Journal of Geophysical Research: Solid Earth 91, 12779-12790.

Faulkner, D. R., C. A. L. Jackson, R. J. Lunn, R. W. Schlische, Z. K. Shipton, C. A. J. Wibberley and M. O. Withjack, 2010. A review of recent developments concerning the structure, mechanics and fluid flow properties of fault zones. Journal of Structural Geology 32(11): 1557-1575.

Frederichs, T., von Dobeneck, T., Bleil, U., Dekkers, M.J., 2003. Towards the identification of siderite, rhodochrosite, and vivianite in sediments by their low-temperature magnetic properties. Physics and Chemistry of the Earth, Parts A/B/C 28, 669-679.

Geng, Z., Bonnelye, A., Chen, M., Jin, Y., Dick, P., David, C. and Schubnel, A., 2017. Elastic anisotropy reversal during brittle creep in shale, Geophys. Res. Lett., 44, 121, 10887-10895.

Guglielmi, Y., Elsworth, D., Cappa, F., Henry, P., Gout, C., Dick, P., Durand, J., 2015. In situ observations on the coupling between hydraulic diffusivity and displacements during fault reactivation in shales. Journal of Geophysical Research: Solid Earth 120, 7729-7748.

Han, D.-h., Nur, A., Morgan, D., 1986. Effects of porosity and clay content on wave velocities in sandstones. Geophysics 51, 2093-2107.

Housen, B.A., Banerjee, S.K., Moskowitz, B.M., 1996. Low-temperature magnetic properties of siderite and magnetite in marine sediments. Geophysical Research Letters 23, 2843-2846.

Holtzapffel, T. (1985). Les minéraux argileux : préparation, analyse diffractométrique et détermination. Société Géologique du Nord 12, 1543.

Jaeggi, D., Laurich, B., Nussbaum, C., Schuster, K., & Connolly, P. 2017. Tectonic structure of the "Main Fault" in the Opalinus Clay, Mont Terri rock laboratory (Switzerland). Swiss Journal of Geosciences, 110(1), 67–84. https://doi.org/10.1007/s00015-016-0243-2.

Jelinek, V. (1981). Characterization of the magnetic fabric of rocks. Tectonophysics 79: 63-67.

Lagroix, F. and Y. Guyodo, 2017. A New Tool for Separating the Magnetic Mineralogy of Complex Mineral Assemblages from Low Temperature Magnetic Behavior. Frontiers in Earth Science 5(61).

Laurich, B., Urai, J. L., Vollmer, C., and Nussbaum, C., 2018. Deformation mechanisms and evolution of the microstructure of gouge in the Main Fault in Opalinus Clay in the Mont Terri rock laboratory (CH), Solid Earth, 9, 1-24, https://doi.org/10.5194/se-9-1-2018.

Lefèvre, M., Guglielmi, Y., Henry, P., Dick, P., Gout, C., 2016. Calcite veins as an indicator of fracture dilatancy and connectivity during strike-slip faulting in Toarcian shale (Tournemire tunnel, Southern France). Journal of Structural Geology 83, 73-84.

Lerouge, C., Grangeon, S., Fléhoc, C., Buschaert, S., Mazurek, M., Matray, J.-M., Tournassat, C., 2012. Diagenetic carbonates in clay-rich marine formations, International meeting "Clays in Natural and Engineered Barriers for Radioactive Waste Confinement", Montpellier, France.

Louis, L., T.-M. Natalie Chen, C. David, P. Robion, T.-f. Wong and S.-r. Song, 2008. Anisotropy of magnetic susceptibility and P-wave velocity in core samples from the Taiwan Chelungpu-Fault Drilling Project (TCDP). Journal of Structural Geology 30(8): 948-962.

Mattei, M., F. Speranza, A. Argentieri, F. Rossetti, L. Sagnotti and R. Funiciello, 1999. Extensional tectonics in the Amantea basin (Calabria, Italy): a comparison between structural and magnetic anisotropy data. Tectonophysics 307(1): 33-49.

Mattei, M., Sagnotti, L., Faccenna, C., Funiciello, R., 1997. Magnetic fabric of weakly deformed clay-rich sediments in the Italian peninsula: Relationship with compressional and extensional tectonics. Tectonophysics 271, 107-122.

Matray, J. M., S. Savoye and J. Cabrera, 2007. Desaturation and structure relationships around drifts excavated in the well-compacted Tournemire's argillite (Aveyron, France). Engineering Geology 90(1): 1-16.

Mennessier, G., and P. Collomb, 1983, Carte géologique de la France 1/50000—Millau Larzac Ouest-Roquefort, Bur. Rech. Géol. et Minières, Orléans, France.

677 Moore D.M., Reynolds R.C., 1989. X-ray diffraction and the identification and analysis of
678 clay minerals. Oxford University Press, - New York.

679 Muxworthy, A.R., Williams, W., 2009. Critical superparamagnetic/single-domain grain sizes
680 in interacting magnetite particles: implications for magnetosome crystals. Journal of The
681 Royal Society Interface 6, 1207-1212.

682 Özdemir, Ö., Dunlop, D.J., Moskowitz, B.M., 2002. Changes in remanence, coercivity and
683 domain state at low temperature in magnetite. Earth and Planetary Science Letters 194, 343-
684 358.

685 Parés, J. M., 2004. How deformed are weakly deformed mudrocks? Insights from magnetic
686 anisotropy. Geological Society, London, Special Publications 238(1): 191-203.

687 Parés, J.M., 2015. Sixty Years of Anisotropy of Magnetic Susceptibility in deformed
688 sedimentary rocks. Frontiers in Earth Science 3.

689 Parés, J.M., van der Pluijm, B.A., Dinarès-Turell, J., 1999. Evolution of magnetic fabrics
690 during incipient deformation of mudrocks (Pyrenees, northern Spain). Tectonophysics 307, 1-
691 14.

692 Parés, J. M., N. J. C. Hassold, D. K. Rea and B. A. van der Pluijm, 2007. Paleocurrent
693 directions from paleomagnetic reorientation of magnetic fabrics in deep-sea sediments at the
694 Antarctic Peninsula Pacific margin (ODP Sites 1095, 1101). Marine Geology 242(4): 261-
695 269.

696 Peyaud, J.-B., Pagel, M., Cabrera, J., Pitsch, H., 2006. Mineralogical, chemical and isotopic
697 perturbations induced in shale by fluid circulation in a fault at the Tournemire experimental
698 site (Aveyron, France). Journal of Geochemical Exploration 90, 9-23.

699 Rahe, B., D. A. Ferrill and A. P. Morris, 1998. Physical analog modeling of pull-apart basin
700 evolution.Tectonophysics 285(1): 21-40.

701 Rochette, P., Fillion, G., Dekkers, M.J., 2011. The Low-Temperature Magnetic Transition of
702 Monoclinic Pyrrhotite. The IRM Quaterly 21.

703 Rochette, P., Fillion, G., Mattei, J.L., Dekkers, M.J., 1990. Magnetic transition at 30-34 K in
704 pyrrhotite-insigth into a widespread occurence of this mineral in rocks. Earth and Planetary
705 Science Letters 98, 319-328.

706 Rossetti, F., Aldega, L., Tecce, F., Balsamo, F., Billi, A., Brilli, M., 2011. Fluid flow within
707 the damage zone of the Boccheggiano extensional fault (Larderello–Travale geothermal field,
708 central Italy): Structures, alteration and implications for hydrothermal mineralization in
709 extensional settings. Geological Magazine 148, 558-579.

710 Savoye, S., Michelot, J.L., Altinier, M.V., Lemius, S., 2008. Origin of pore-water isotopic
711 anomalies near fractures in the tournemire shales. Physics and Chemistry of the Earth, Parts
712 A/B/C 33, Supplement 1, S87-S94.

713 Sellin, P. and O. X. Leupin, 2013. The use of clay as an engineered barrier in radioactive-
714 waste management – a review. Clays and Clay Minerals 61(6): 477-498.

715 Singsoupho, S., T. Bhongsuwan and S.-Å. Elming, 2015. Palaeocurrent direction estimated in
716 Mesozoic redbeds of the Khorat Plateau, Lao PDR, Indochina Block using anisotropy of
717 magnetic susceptibility. Journal of Asian Earth Sciences 106: 1-18.

718 Smirnov, A., 2009. Grain size dependence of low-temperature remanent magnetization in
719 natural and synthetic magnetite: Experimental study. Earth, Planets and Space 61, 119-124.

720 Verwey, E. J. W. (1939). "Electronic Conduction of Magnetite (Fe3O4) and its Transition
721 Point at Low Temperatures." Nature 144: 327.

Figure (with caption below and on the same page)

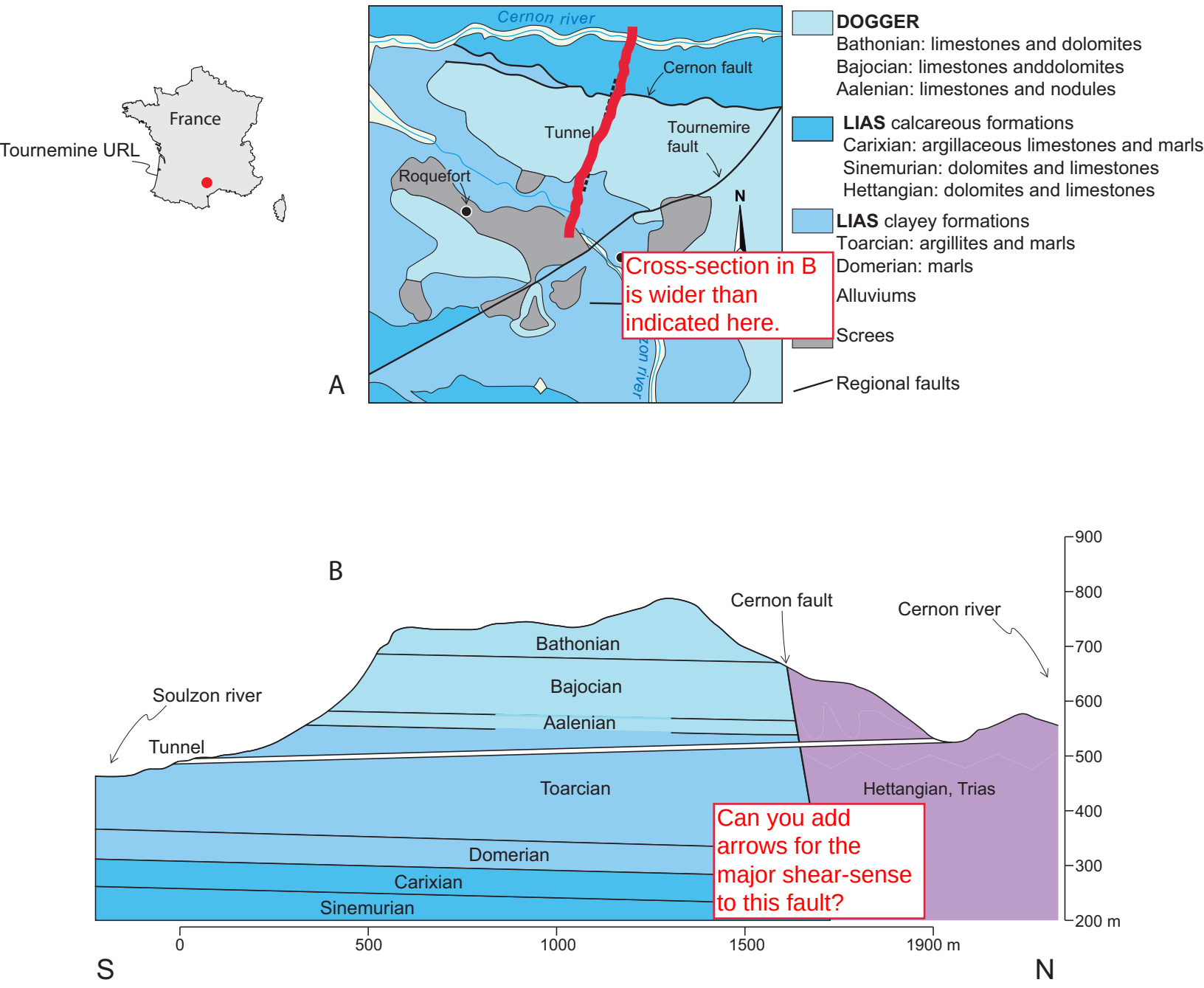

Figure 1: (A) Location of the Tournemire site: simplified geological map after Mennessier and Collomb (1983). (B) Geological cross-section of the Tournemire experimental station (Cabrera, 2002).

Figure (with caption below and on the same page)

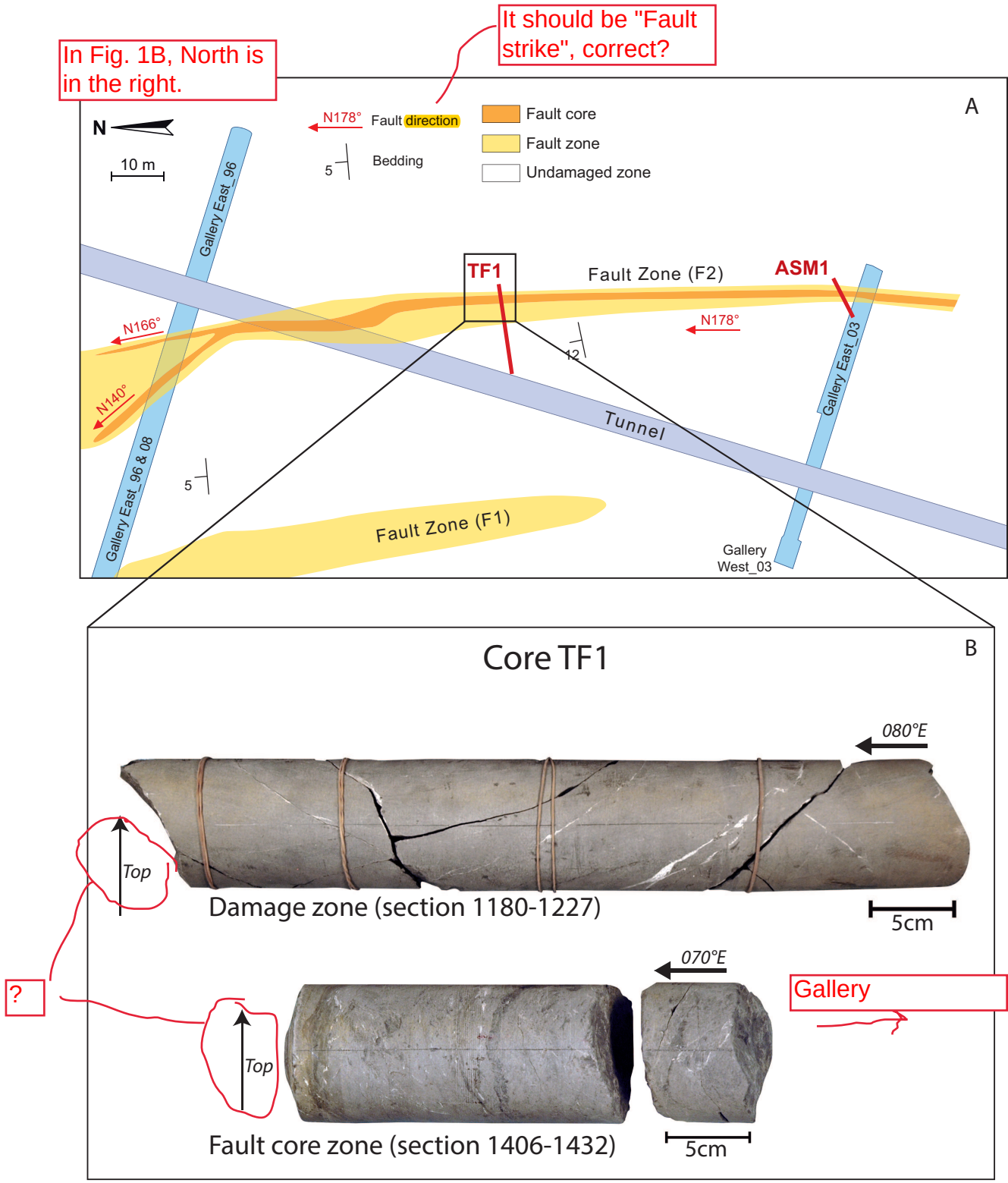

Figure 2: (A) Simplified map of the Tournemire Underground Research Laboratory and cores TF1 and ASM1 location (Dick et al. 2016). (B) Picture of sections 1180-1227 (damage zone) and 1406-1432 (fault core) from TF1.

Figure (with caption below and on the same page)

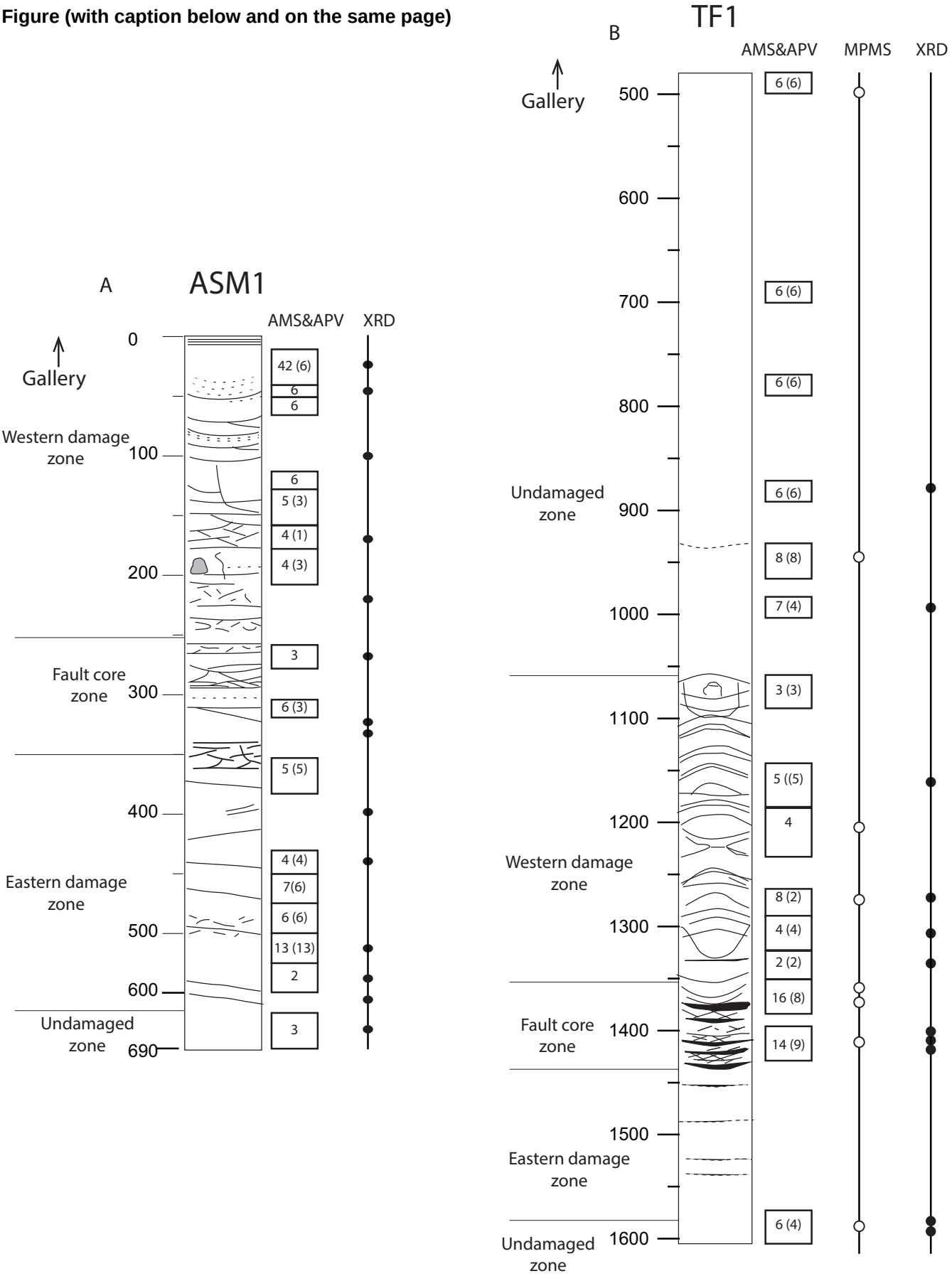

Figure 3: Logs of ASM1 (A) (société Martinez and Pierre Dick, personal communication) and TF1 (B) (Cofor - GeoSonic France for the IRSN) made during the drilling process. The spatial distribution of the undamaged, damage and fault core zones was determined on observation criteria during the core logging. The number cubes for ASM and (APV) are indicated. The black and white circles correspond respectively to the near shear points in where the powder samples were collected for the XRD and low-T SIRM measurements.

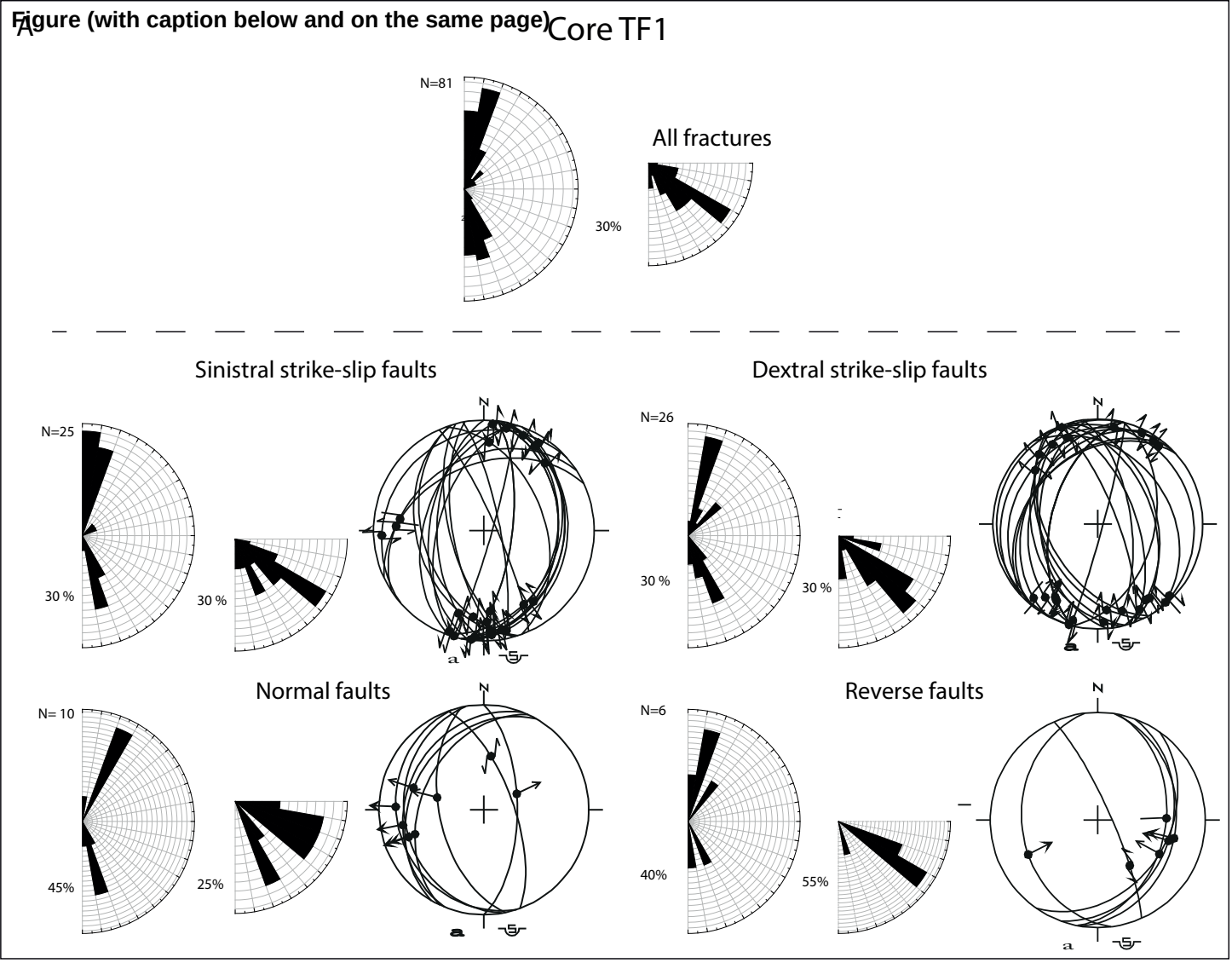

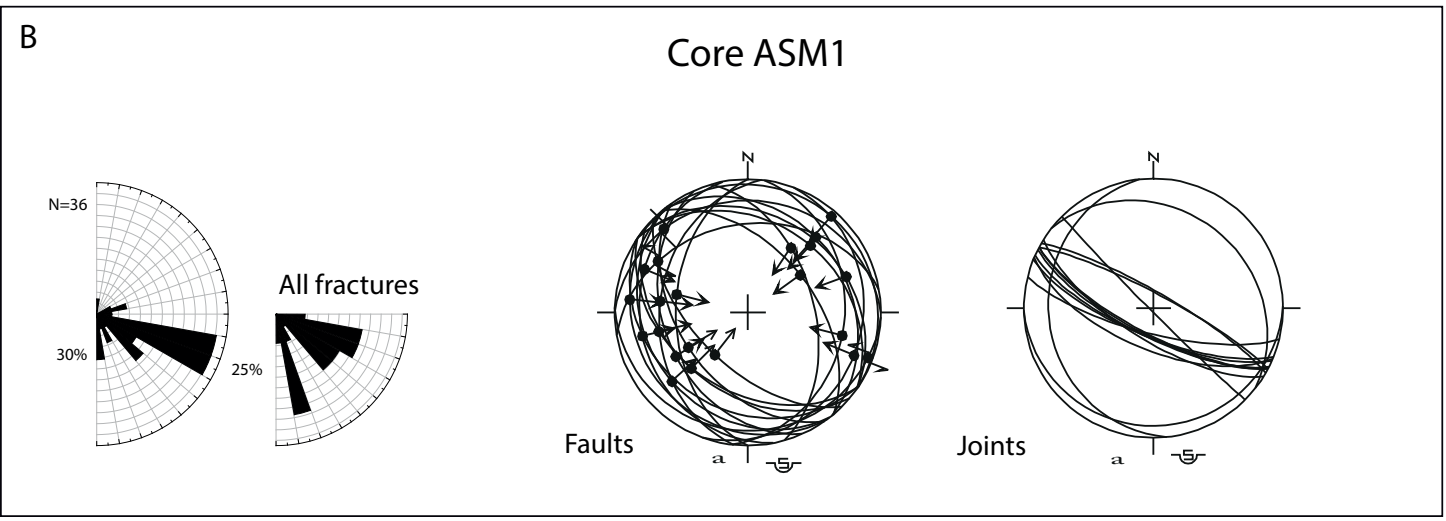

Figure 4: Stereographic projection (lower hemisphere, equal-area projection) showing the orientation and striae of the fault planes measured in TF1 and ASM1 cores. (A) Rose diagrams of the fault strike and fault dip for all the fractures in core TF1. Rose diagrams and paleo-stress orientation determined by slickensides analyses for: Sinistral strike-slip faults, dextral strike-slip faults, normal faults and reversal faults. (B) Rose diagrams of the fault strike and fault dip in core ASM1. Paleo-stress orientation determined by slickensides analyses for faults and joints. Lines: fault planes. Slickenside lineations in dots with double arrows for strike-slip motion and with outward-directed or inward-directed single arrow for normal or reverse motion. The fault surfaces measured in F2 fault zone show a main N-S trend, but various orientation and sense of the slip vector. See in text for further explanation.

Figure (with caption below and on the same page)

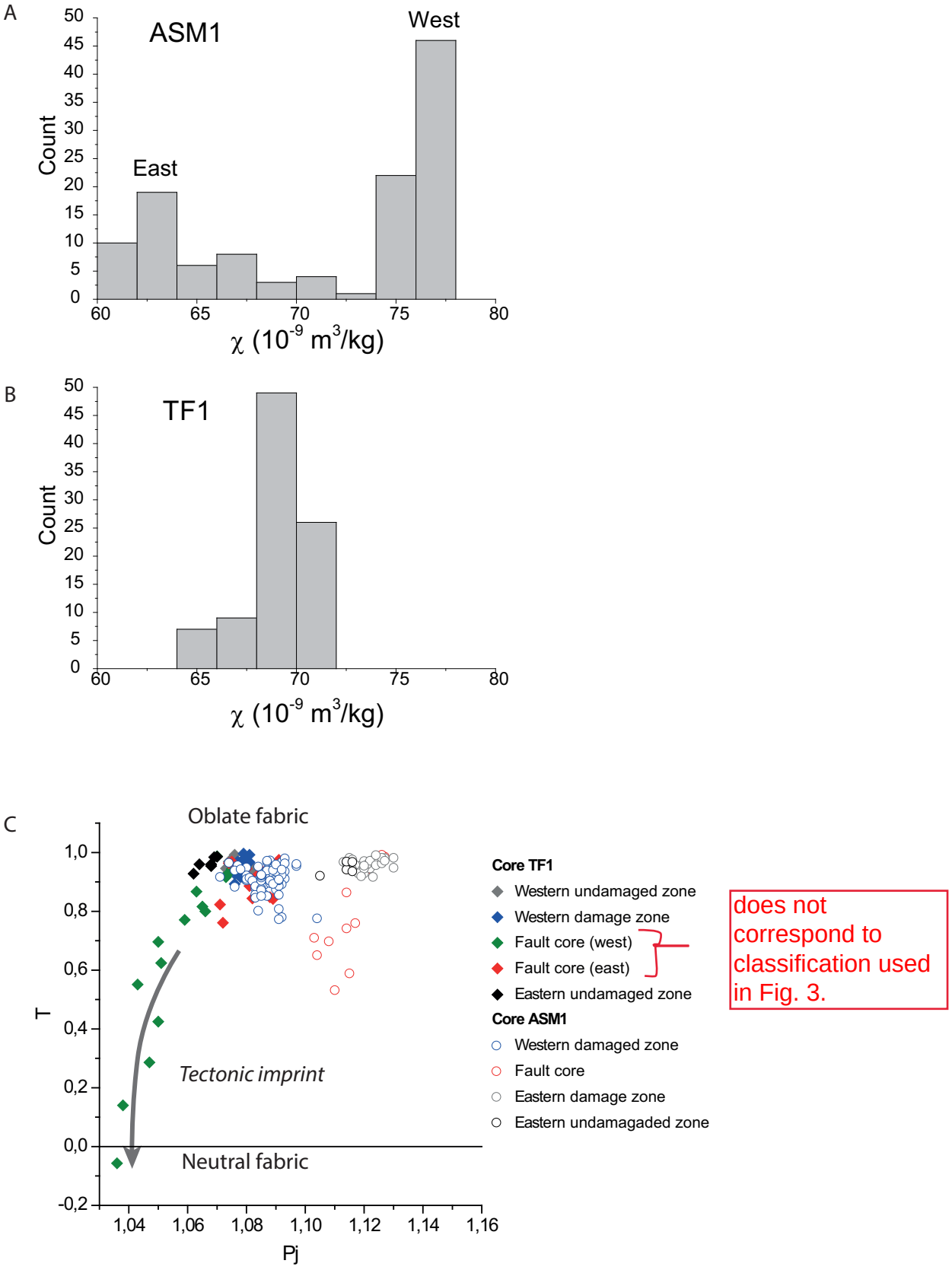

Figure 5: Histogram of density normalised magnetic susceptibility for cores ASM1 (A) and TF1 (B)). Jelinek diagram for cores TF1 and ASM1 showing the evolution of the ASM shape parameter (T) versus the degree of anisotropy (Pj) (C).

Figure (with caption below and on the same page)

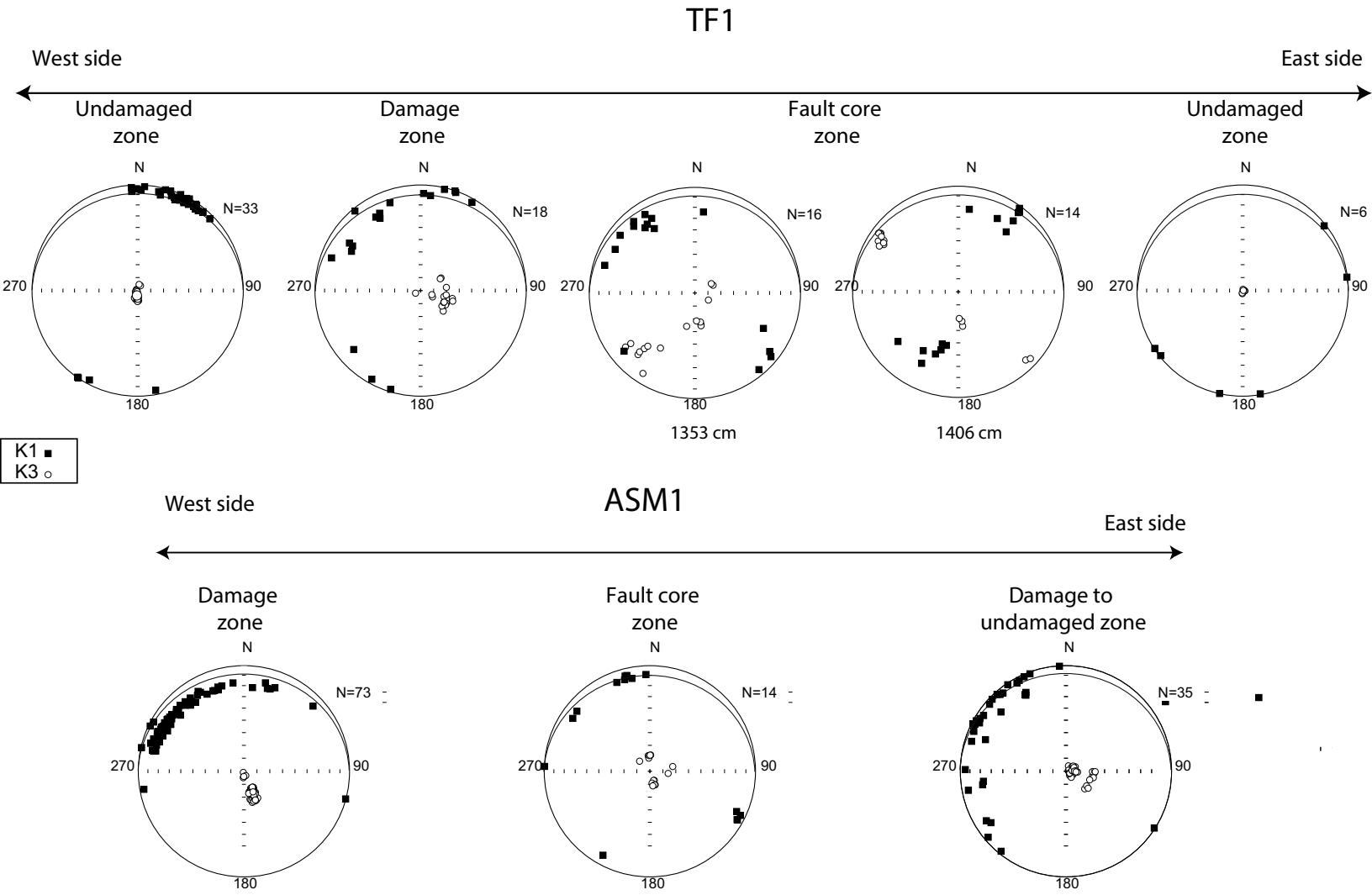

Figure 6: Equal-area lower-hemisphere stereograms in geographical coordinate system of the principal AMS axes for the undamaged zone, damage zone and fault core zone of cores TF1 and ASM1. White circles represent K3 axes, triangles and black squares represent K1 axes. The black line represents a bedding plane oriented to the north with a 10°dip which corresponding to the values measured in the undamaged zone.

Figure (with caption below and on the same page)

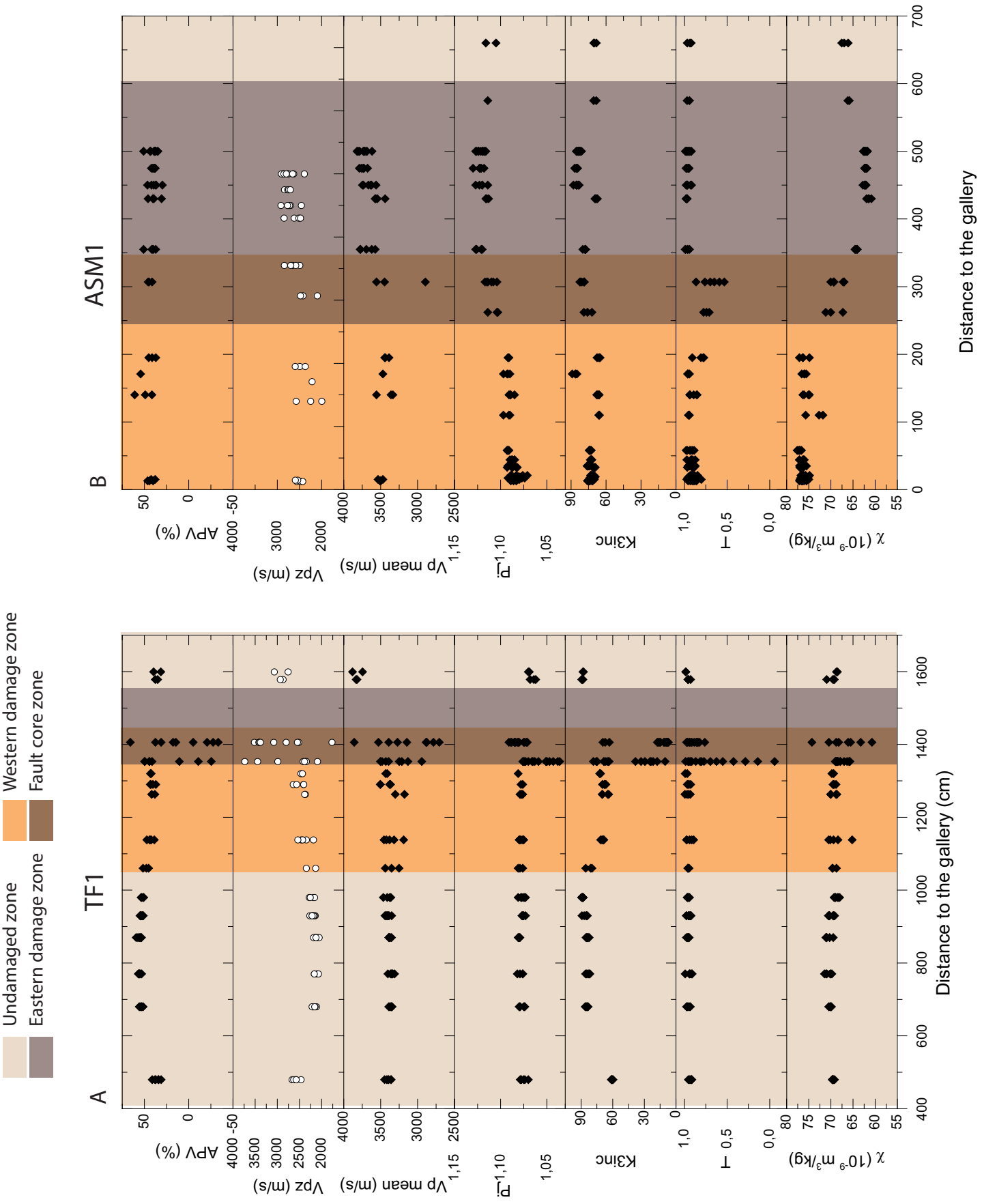

Figure 7: Evolution of magnetic susceptibility normalized by the density (m3/kg), shape parameter T, degree of anisotropy Pj; K3 inclination, mean Pp (Vpm=(Vpx+Vpy)/2); Vpz (m/s) and % APV for core TF1 (A) and ASM1 (B) across the undamaged, damage and the fault core zones.

Figure (with caption below and on the same page)

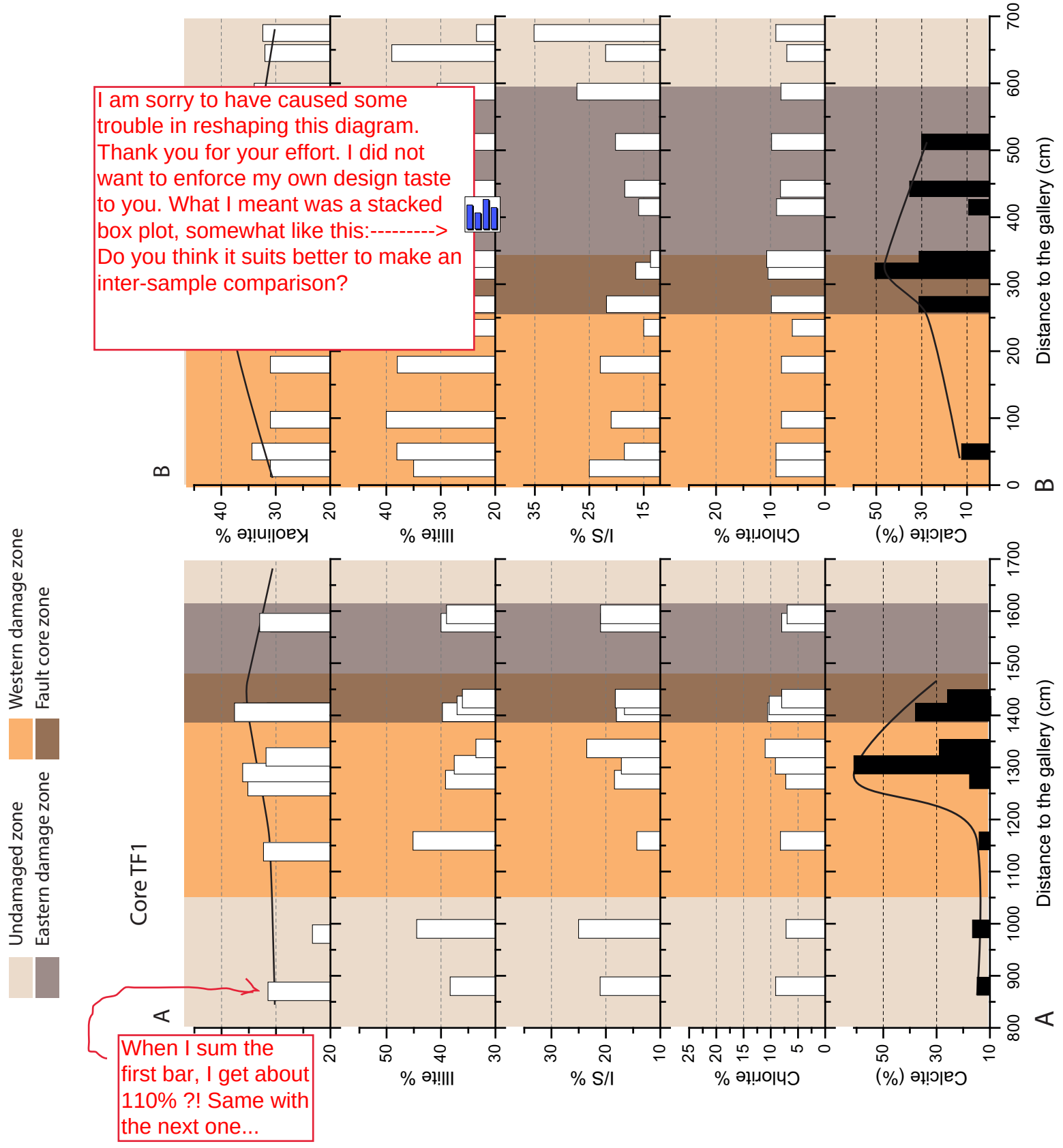

Figure 8: Stacked box plot indicating the relative proportions of calcite and of the various clay minerals in cores TF1 and ASM1 across the undamaged, damage and the fault core zones. The main trend observed in calcite and kaolinite measurements is indicated by a black line.

Figure (with caption below and on the same page) TF1 980-1000 cm

A

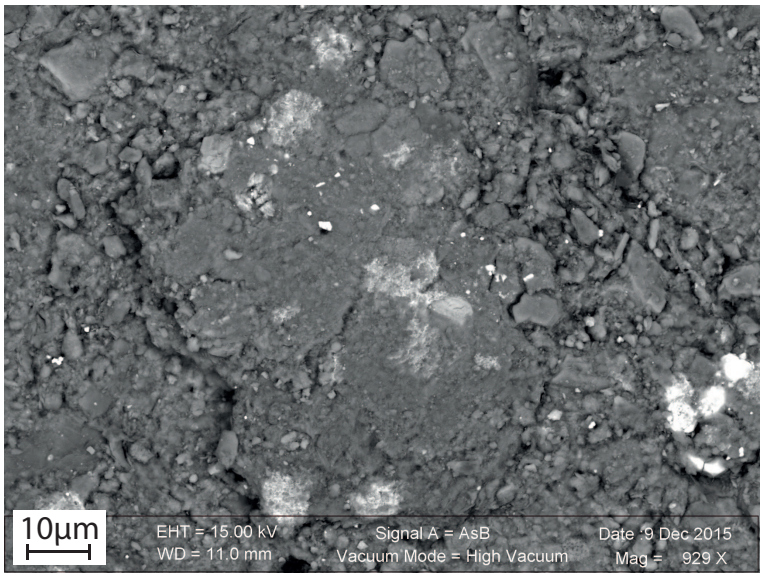

B

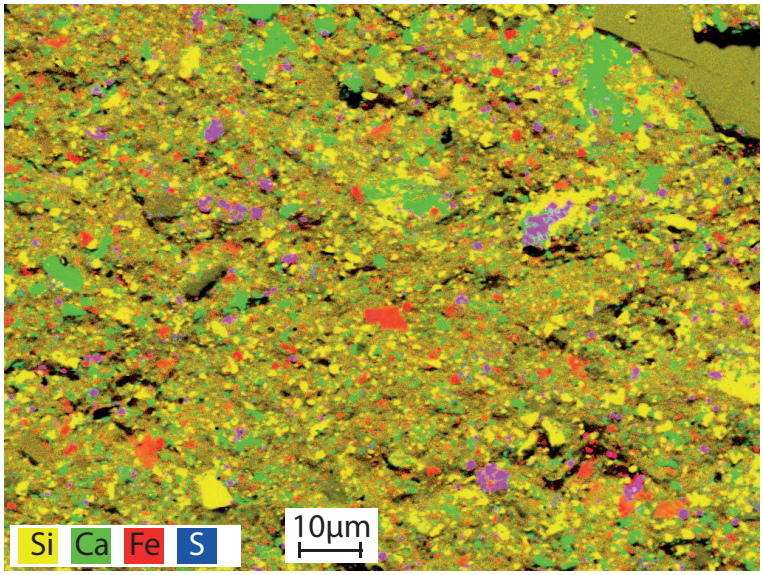

C

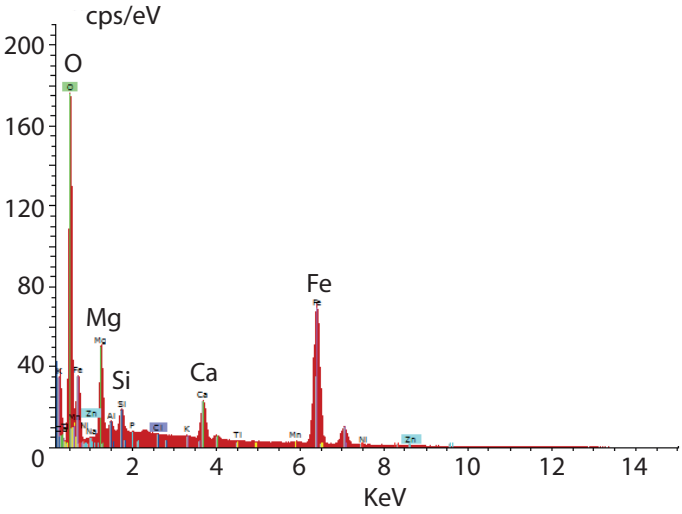

I do not think that this figure is necessary. It would be nice if there were a comparison between samples, e.g. from the damaged zone or the fault core.

Figure 9: (A) SEM image of a broken surface in core TF1, section 980-1000 (undamaged zone). (B) Si, S, Fe, Ca elements mapping of the same sample. Silicates, calcites, pyrites and small quantities of iron carbonates were observed. (C) EDS spectrum of iron reach carbonate observed in SEM image.

Figure (with caption below and on the same page)

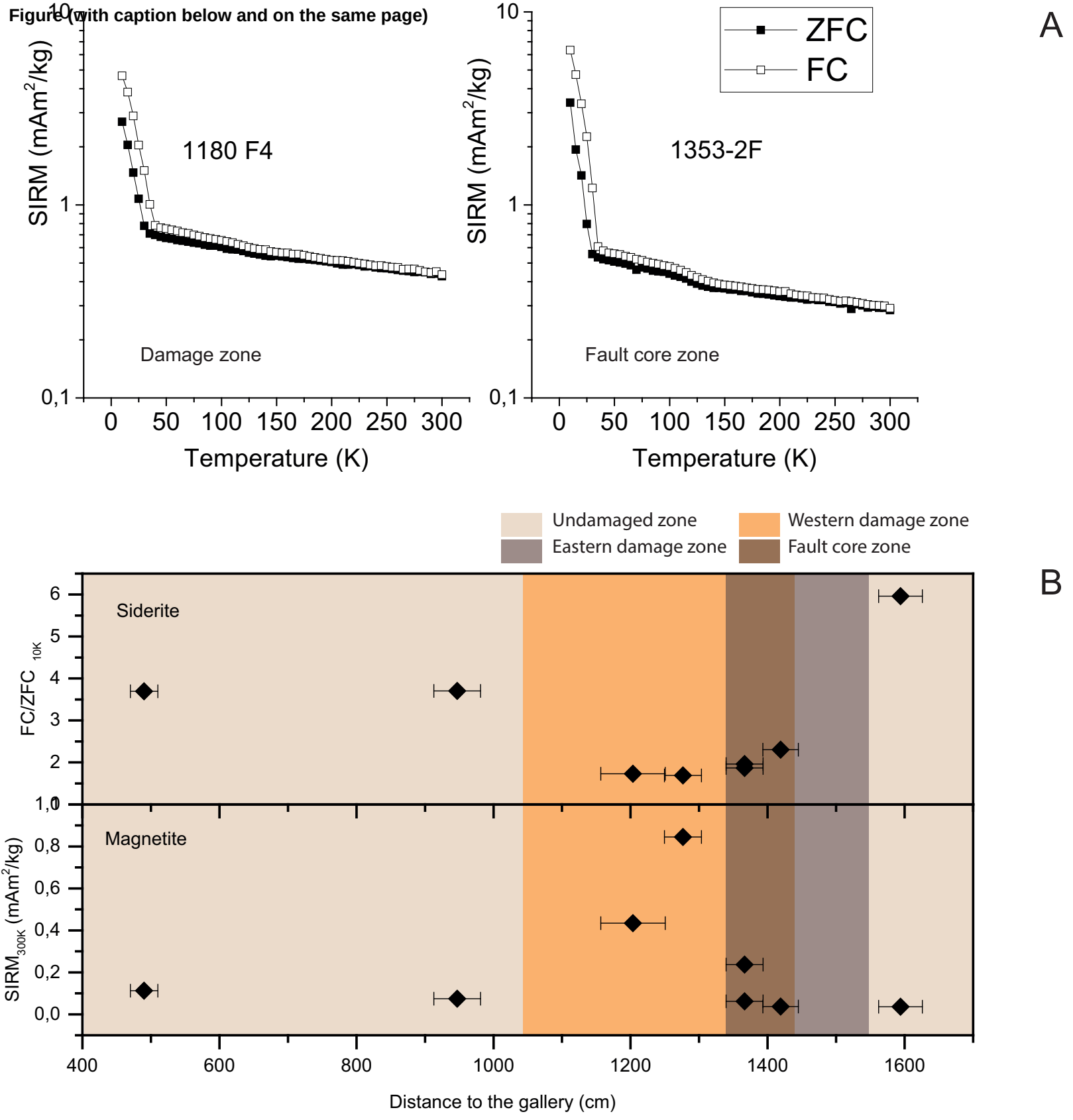

Figure 10: LT-SIRM warming curves measured in powders from the fracture planes in the damage zone (sample 1180) and fault core zone (sample 1353) in core TF1. FC (Field cool) and ZFC (Zero field curve) correspond respectively to samples cooled at zero field and a field of 2.5T. (B) Evolution of the SIRM at room temperature ($SIRM_{300K}$) and FC/ZFC ratio at 10K across the undamaged, damage and the fault core zones.

Figure (with caption below and on the same page)

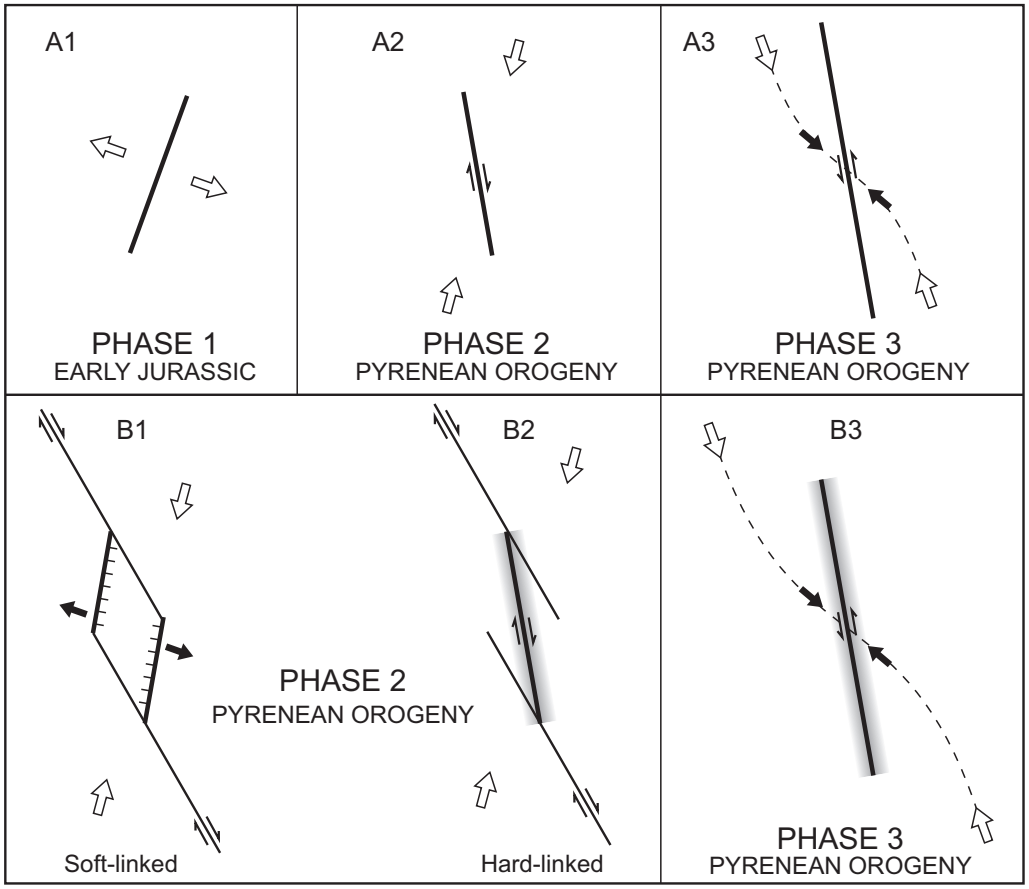

Figure 11: Alternative scenario for the time evolution of F2 fault zone in the Tournemire Gallery. In A, F2 fault first formed as a normal fault during the Early Jurassic extensional tectonics (A1) and was later reactivated during the Pyrenean orogeny. Due to the counterclockwise rotation of the Pyrenean compression through time, F2 first slipped as a dextral fault (A2) and then as a sinistral fault (A3). In B, all fractures found in F2 zone resulted from its strike-slip movement during the Pyrenean orogeny. B1 and B2 represent the evolution of a relay between two NW-SE dextral fault segments. Normal faulting in this extensive relay was followed by branching of the two faults segments. Sinistral reactivation then occurred (B3) as the Pyrenean compression rotated counterclockwise as in A3.